Spatial Organization of Astrocytes in Ferret Visual Cortex

Mónica López-Hidalgo, Walter B. Hoover, and James Schummers*

Max Planck Florida Institute for Neuroscience, Jupiter, Florida 33458

ABSTRACT

Astrocytes form an intricate partnership with neural circuits to influence numerous cellular and synaptic processes. One prominent organizational feature of astrocytes is the "tiling" of the brain with non-overlapping territories. There are some documented species and brain region–specific astrocyte specializations, but the extent of astrocyte diversity and circuit specificity are still unknown. We quantitatively defined the rules that govern the spatial arrangement of astrocyte somata and territory overlap in ferret visual cortex using a combination of in vivo two-photon imaging, morphological reconstruction, immunostaining, and model simulations. We found that ferret astrocytes share, on average, half of their territory with other astrocytes. However, a specific class of astrocytes, abundant in thalamo-recipient cortical layers ("kissing" astrocytes), overlap markedly less. Together, these results demonstrate novel features of astrocyte organization indicating that different classes of astrocytes are arranged in a circuit-specific manner and that tiling does not apply universally across brain regions and species. J. Comp. Neurol. 524:3561–3576, 2016.

INDEXING TERMS: astrocyte territories; tiling; overlap; two-photon; AB_306716; AB_2298772; AB_1587626; AB_397473; nif-0000-00314

Astrocytes are multifunctional brain cells that have been implicated in a wide array of important brain functions, including the provision of trophic factors, structural and metabolic support to neurons (Molofsky et al., 2012; Tsai et al., 2012; Clarke and Barres, 2013; Sloan and Barres, 2014), regulation of vascular tone (Filosa et al., 2015; Kim et al., 2015), neurovascular coupling (Attwell et al., 2010; Petzold and Murthy, 2011; Otsu et al., 2015), ion and transmitter clearance (Rose and Karus, 2013; Sibille et al., 2014, 2015; Tong et al., 2014; Murphy-Royal et al., 2015), and direct communication with neurons via gliotransmission (Jourdain et al., 2007; Henneberger et al., 2013; Shigetomi et al., 2013; Araque et al., 2014). Astrocyte interactions with neural elements are important for normal brain development, ongoing function, and plasticity, although many specific mechanistic hypotheses remain controversial (Agulhon et al., 2010; Petravicz et al., 2014; Srinivasan et al., 2015).

One of the prominent features of astrocyte organization, well characterized in the hippocampus, is the so-called tiling of neural tissue. In this scheme, astrocyte somata are evenly distributed and their processes overlap only minimally, such that each astrocyte covers an exclusive territory of neuropil. In careful studies in rat hippocampus, it was shown that the processes of neighboring astrocytes exhibit minimal spatial overlap (Bushong et al., 2002, 2004; Wilhelmsson et al., 2006). A similar organization has been described in other species and brain regions (Grosche et al., 2002; Oberheim et al., 2006; Halassa et al., 2007; Stork et al., 2014). Although this tiling arrangement has become the standard model for astrocyte organization, the majority of our understanding of gray matter astrocytes derives

Grant sponsor: The Max Planck Society.

Dr. López-Hidalgo's current address: Universidad Autónoma de Querétaro, Facultad de Medicina, Clínica del Sistema Nervioso, 76010 Santiago de Querétaro, Querétaro, Mexico

*CORRESPONDENCE TO: James Schummers, Max Planck Florida Institute for Neuroscience, 1 Max Planck Way, Jupiter FL 33458. E-mail: james.schummers@mpfi.org

Received December 14, 2015; Revised April 1, 2016;
Accepted April 4, 2015.
DOI 10.1002/cne.24015
Published online August 11, 2016 in Wiley Online Library (wileyonlinelibrary.com)

from work in the rodent hippocampus, and information about anatomical arrangement from other brain regions and species is sparse.

The cortex has become a popular neural circuit in which to study astrocyte behavior in vivo (Wang et al., 2006; Schummers et al., 2008; Bonder and McCarthy, 2014; Paukert et al., 2014); however, the spatial organization and morphology of cortical astrocytes have not been thoroughly studied. The visual cortex of the ferret is an attractive model for studying development (Chapman and Stryker, 1993), functional organization of visual receptive fields (Usrey et al., 2003), and neuron–astrocyte interactions (Schummers et al., 2008). As in primates, but unlike rodent visual cortex (Ohki and Reid, 2007; Van Hooser, 2007), ferret visual cortex has a columnar organization, and spatial mapping of visual receptive field properties (Chapman and Stryker, 1993; Weliky et al., 1996; Yu et al., 2005). Visually driven calcium elevations in ferret visual cortex share the receptive field properties of adjacent neurons, and the spatial arrangement of receptive field properties of astrocytes is precisely aligned to the neuronal map, suggesting a fine spatial scale of neuron–astrocyte communication (Schummers et al., 2008). However, the cellular and network organization of astrocytes has not been thoroughly examined in ferret visual cortex.

MATERIALS AND METHODS

Animals

All experimental procedures conformed with NIH Guidelines for the Care and Use of Laboratory Animals and were approved by the Max Planck Florida Institute for Neuroscience IACUC. Young male adult ferrets (P60–P80), old ferrets (1 year old; Marshall Farms, North Rose, NY), and BL6/C57 mice (P40–P100; Jackson Laboratory, Bar Harbor, ME) were used in the present study.

For in vivo imaging experiments, ferrets were pretreated with atropine, and anesthesia was induced with a mixture of ketamine (25 mg/kg) and xylazine (1.5 mg/kg) and maintained during surgical procedures with isoflurane (1.2–1.5% in a 50:50 mixture of N_2O:O_2). The eyes were protected with ophthalmic ointment during the surgery and moistened afterward with silicone oil. A head plate was attached to the skull with dental acrylic, which was mounted on the movable stage of the microscope. $EtCO_2$, heart rate, and spO_2 were monitored continuously to assess depth of anesthesia and general physiological condition of the animals. Body temperature was maintained at 38.5°C with a homeothermic heating blanket with a feedback circuit. A craniotomy and durotomy were performed to expose a large portion of area 17, which was covered with 2% agarose dissolved in artificial cerebrospinal fluid (ACSF). The cortical window was then closed with a glass coverslip and sealed with dental acrylic. A small gap was left between the coverslip and the skull to enable penetration with the electroporation pipette.

Mice were anesthetized with a cocktail containing fentanyl (0.05 mg/kg), midazolam (5 mg/kg), and medetomidine (0.5 mg/kg), supplemented with isoflurane. The eyes were protected with ophthalmic ointment during the surgery and moistened afterward with silicone oil. A metal headplate was attached to the skull using superglue and dental acrylic, and a 2-mm × 2-mm craniotomy was performed over the primary visual cortex region (area 17). The exposed area was then covered with a thin layer of 2% agarose in ACSF and a glass coverslip.

Single-cell electroporation

Young ferrets ($n = 26$), old ferrets ($n = 2$), and mice ($n = 5$) were used. Astrocytes were labeled with sulforhodamine 101 (SR101) by surface application (200 μM). Individual astrocytes were targeted for electroporation with a borosilicate patch-style pipette with resistances between 5 and 7 MOhm, filled with 10,000 MW dextran-conjugated fluorophores (Alexa Fluor 488 or Alexa Fluor 594; 1 mM) dissolved in ACSF. The pipette was directed to close apposition to the astrocyte membrane assessed by live dual-channel two-photon imaging, and confirmed by a small increase in pipette resistance. Upon contact with the cell membrane, single square voltage pulses (500 ms, 1 V) were typically sufficient to fill the astrocytes with the dye. In some cases a second pulse was delivered.

Two-photon imaging

Two-photon imaging was performed with an Ultima IV microscope (Prairie Technologies, Middleton, WI), coupled to a titanium-sapphire laser providing excitation with ~100 fs pulses at 80 MHz (Tsunami; Spectra-Physics, Menlo Park, CA). Fluorescence from the astrocytes electroporated with Alexa Fluor 488 and Alexa Fluor 594 was detected simultaneously using photomultiplier tubes (Hamamatsu, Shizouka, Japan) through a 16×, 0.8 NA objective lens (Nikon). The fluorescence was separated with a 575-nm dichroic mirror, and collected on two channels filtered at 525 ± 35 and 607 ± 22 nm. The laser intensity was at maximum 20 mW and the gain of the photomultiplier tubes was in the range of 590–610 V, avoiding saturation in the pixels of the image. Cross-talk between these channels was never observed, not even at the soma, where the intensity was the highest due to the amount of dye localized

at the cytosol. Image acquisition was accomplished using PrairieView software. We focused our imaging on layer 2, which was readily distinguished from layer 1 on the basis of the negatively stained neurons. This determination was made independently in each experiment, and ranged between 120 and 130 μm from the pial surface.

Immunohistochemistry and histology

Young ferrets ($n = 3$) were deeply anesthetized with sodium pentobarbital (Euthasol) and perfused transcardially with 50 ml of heparinized saline followed by 400 ml of fixative (4% paraformaldehyde in 0.1 M sodium phosphate-buffered saline [PBS], pH 7.4). The brains were removed and postfixed in a 4% paraformaldehyde 0.1 M PBS solution at 4°C for 24 hours. Then 50 mm parasagittal sections were collected in 0.1 M PBS (pH 7.4) using a vibrating microtome and stored at 4°C. Sections for immunoprocessing were incubated for 60 minutes at room temperature (RT) in 5% normal goat serum (NGS, Jackson ImmunoResearch, West Grove, PA, cat. # 005-000-121) to block nonspecific labeling and incubated for 48 hours at room temperature in a cocktail of primary antibodies and diluent (1% NGS in PBS containing 0.25% Triton X-100, pH 7.4). Primary antibodies were as follows: rabbit anti- S100 (Abcam, Cambridge, MA, cat. #ab868, 1:500, AB Registry ID: AB_306716), mouse monoclonal anti-NeuN (Millipore, Billerica, MA, cat. #MAB377, 1:5000, AB Registry ID: AB_2298772), guinea pig anti-vesicular glutamate transporter 2 (VGlut2; Millipore, cat. #AB2251, 1:5000, AB Registry ID: AB_1587626), and mouse monoclonal anti-Connexin 43 (BD Biosciences, Franklin Lakes, NK, cat. #610061, 1:5,000, AB Registry ID: AB_397473). After the primary incubation, sections were washed in PBS (5 × 3 minutes) and then incubated for 3 hours in a cocktail of secondary antibodies conjugated to Alexa Fluor dyes (Life Technologies, Carlsbad, CA) to tag the primary antibodies at a concentration of 1:500. Goat anti-rabbit Alexa 488 and Goat anti-mouse Alexa 594 were used to detect S100 and NeuN. Following secondary antibody immunostaining, tissues were washed, incubated in Hoechst solution (1:20,000) and saline (pH of 7.4) for 6 minutes, and washed 3 times in PBS to stop Hoechst staining. Stained sections were mounted onto Superfrost (VWR, Radnor, PA, cat. #48311-703) slides, coverslipped using Slow Fade Gold Antifade media (Life Technologies, cat. #S36936) and stored at 4°C.

Antibody characterization

The S100 antiserum recognized a band between 21 and 24 kDa on western blots of ferret brain. Immunostaining of ferret and mouse cortex revealed the expected pattern of staining (see Fig. 2) matching morphologically to astrocytes and not overlapping with NeuN staining (Yasuda et al., 2004).

The NeuN antiserum recognized bands at 46, 48, and 66 kDa, on western blots of ferret brain, consistent with the manufacturer's documentation. Immunostaining in mouse and ferret cortex revealed a pattern of nuclear staining consistent with laminar neuronal cell density patterns, and complementary to S100 staining (see Fig. 2).

The VGlut2 antiserum recognized bands at 42 and 52kDa on western blots of ferret brain, consistent with the manufacturer's documentation. Immunostaining in ferret cortex revealed a pattern identical to previous reports, namely, thin fibers of an axonal appearance with the highest density in layers 4 and 3 of cortex (Nahmani and Erisir, 2005), consistent with the established pattern of thalamocortical projections.

The Connexin 43 antiserum recognized bands at 43 and 50 kDa on western blots of ferret brain, consistent with the unphosphorylated and phosphorylated forms of the protein (Granot and Dekel, 1994). Immunostaining in ferret cortex revealed the expected pattern of expression as in previous reports in cortex (Mei et al., 2010; Theodoric et al., 2012), as well as the distinctive laminar pattern in the cerebellum (Koster-Patzlaff et al., 2008).

Confocal imaging

Fixed tissue was imaged with a Zeiss LSM780 confocal microscope (Carl Zeiss MicroImaging) using a Zeiss plan-Apochromat 40×/1.3 oil objective (NA 1.3). Fluorophores were excited with an Argon laser at 458, 488, and 514 nm (for 488 nm), an HeNe laser at 633 nm (for 647nm), a DPSS laser at 561 nm (for 555 nm), an HeNe laser at 594 nm (for 594 nm), and a laser Diode at 405 nm (for 405 nm). To compute the number of astrocytes (S100+) and neurons (NeuN+) as well as the location of vGlut2, z-stacks were acquired with steps of 2 μm and a pixel size of 0.5 × 0.5 μm. When Cx43 was imaged, z-stacks were acquired with 1-μm steps and a pixel size of 0.1 × 0.1 μm.

Data analysis

Reconstruction and volume calculations

Quantification of volumes of astrocytes electroporated in vivo was performed using z-stacks obtained with a two-photon microscope. Z-stacks were acquired with steps of 2 μm covering the entire astrocyte and with a pixel size of ~0.3 × 0.3 μm. To obtain volume measurements, 3D surfaces were generated with Surface Module of IMARIS software (IMARIS 7.71; Bitplane, RRID:nif-0000-00314). Briefly, the intensity of the

channel was use to fit triangles to render the image. The threshold was determined for each astrocyte and visually inspected to confirm the representation of the entire astrocyte. When multiple astrocytes were electroporated, contiguous astrocytes were filled alternating Alexa 488 and Alexa 594 to avoid cross-talk with the channels. For overlapping quantification, the astrocytes were extracted in individual channels, and the surface of an astrocyte was use to mask the channel of a neighboring astrocyte. The amount of overlap was considered as the signal located in the same physical space in two channels.

Cell counting

Neuron and astrocyte soma locations were identified based on NeuN and S100 staining of 50-μm parasagittal sections. Confocal image stacks were tiled to generate mosaics covering ~1 mm in the anteroposterior plane and 2 mm in the coronal plane, through all cortical layers.

Neuronal somata were automatically identified using Surface Module of IMARIS software (IMARIS 7.71; Bitplane) and extracted to a table of [x,y,z] coordinates. Laminar boundaries were automatically identified based on density of cell bodies with custom routines written in Matlab. For this calculation, soma locations from two to three consecutive 50-μm sections were aligned and collapsed across the z-plane (coronal) using the pial surface as a reference. The local density in a sliding 25-μm window was computed to generate a density image. The stereotypical changes in density, alternating low–high from layers 1–6 were identified by finding the peaks in the derivative of the density in 25-μm sliding windows, corresponding to the transitions from high-to-low or low-to-high density.

Because astrocyte somata were more difficult to automatically identify due to their heterogeneous shape and variable intensity of S100 within primary processes, they were identified by custom routines written in Matlab. Images were preprocessed by high-pass spatial filtering followed by adaptive image histogram equalization to compensate for uneven spatial distribution of the S100 stain. Putative cell bodies were automatically identified by thresholding, and segmentation, subject to exclusion based on size and ellipticity criteria. Putative cell bodies with large aspect ratios or volumes were identified for evaluation by visual inspection. Kissing astrocytes were visually identified, and center positions were marked manually, based on confirmation with the Hoechst channel. It is of note that, due to the complex morphology and the extremely high intensity of staining for S100 of layer 1 astrocytes, identification of layer 1 astrocytes was often ambiguous. For this reason, layer 1 astrocytes were excluded from analysis in the figures, except for Figure 2B and Figure 3C.

Model and simulations

All modeling was performed using in-house routines written in the Matlab environment. The curve for overlap volume versus intersomatic distance was fit with a single exponential curve by least-squares minimization. For every S100+ astrocyte (n = 4,904), the 3D cardinal distance was computed to every other astrocyte within 55 μm, to build a table of all n neighbors for each center cell. For each of these neighbors, the exponential fit was evaluated to compute the predicted overlap for the corresponding distance. Cells with a distance less than 15 μm were assigned the mean value for all kissing pairs (see Fig. 6C). The volume of overlap for each of the n neighbors was then summed to compute the "Total Overlap" for each center cell. This value was then converted to the predicted exclusive territory value: 100 − (Total Overlap/mean astrocyte volume).

Simulation of overlap with spherical territories was performed as follows. For each reconstructed astrocyte (n = 73), the volume (Fig. 1D) was converted to the equivalent radius for a sphere of the same volume. The distribution of these radii was fit with a Gaussian function (Fig. 7A). Then, each astrocyte in the S100+ population was assigned a radius by drawing randomly from the fitted Gaussian distribution. The overlap between each cell pair was then computed analytically from the overlap of the two spheres. Subsequent processing was the same as for the real data. The total overlap for each cell was computed as the sum of overlap from all neighbors (Figure 7B).

RESULTS

Astrocyte processes are extensively ramified, and the thinnest processes are extremely fine in caliber. To characterize the extent of the territories covered by these processes, we electroporated individual layer 2 astrocytes in vivo with fluorescent dyes under visual guidance of two-photon imaging of SR101 staining (Fig. 1A). The morphology of each astrocyte was reconstructed from image z-stacks collected by in vivo two-photon microscopy. All of the hallmarks of protoplasmic astrocytes were evident in these reconstructions (Fig. 1B); each cell had a small soma, and several primary processes, which ramified to branches and branchlets. Each astrocyte had at least one process that terminated in a structure that had the morphological characteristics of a perivascular endfoot. The overall size and shape of the territories was quite diverse, with overall elongations (aspect ratios > 1.0), complex

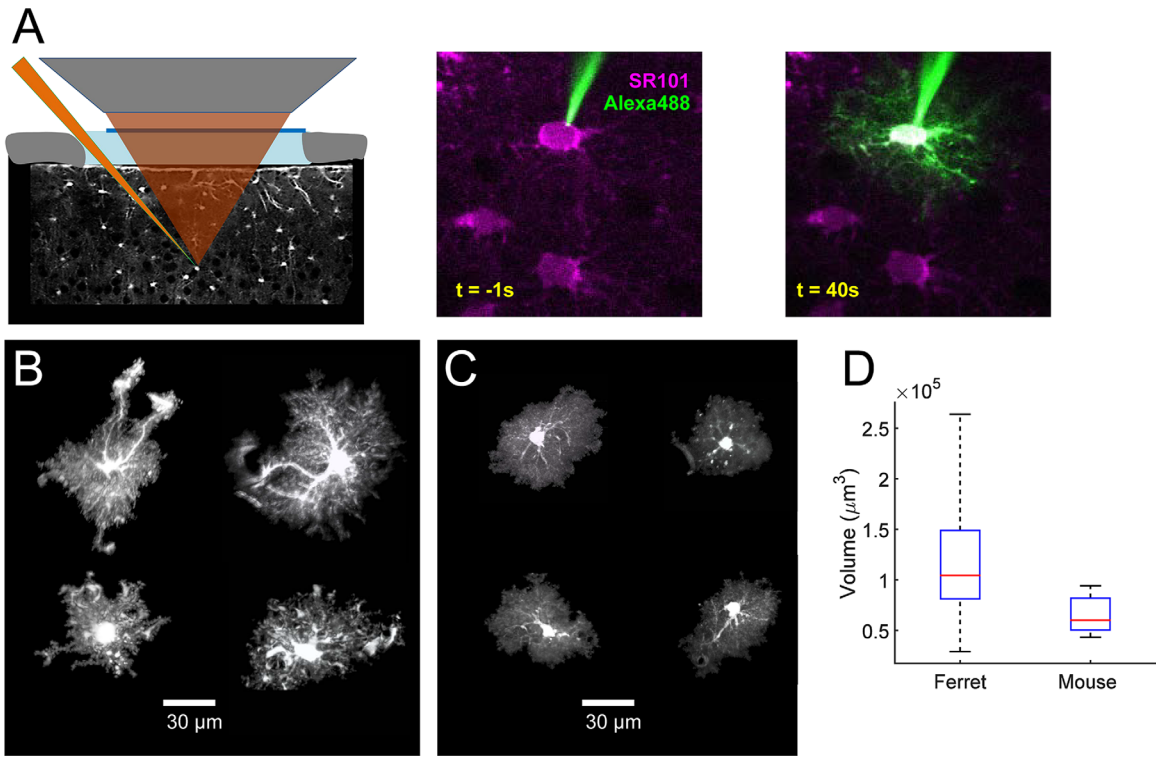

Figure 1. Astrocyte territory volume. **A:** Left: schematic showing two-photon guided single-cell electroporation of SR101-positive astrocytes. Right: example of electroporation process. **B:** Examples of the diversity of ferret astrocyte morphology. Each image is a projection generated from 3D reconstruction of the z-stack. Volumes, clockwise from top left: 107,524; 98,861; 118,048; 54,614. **C:** Examples of the morphology of mouse astrocytes. Volumes, clockwise from top left: 54,117; 46,735; 47,023; 48,671. **D:** Boxplot showing comparison of territory volumes between ferret and mouse astrocytes. Boxplots represent the median and interquartile range (25th and 75th percentile), and whiskers represent the minimum and maximum values. Scale bar = 30 µm in B,C.

invaginations, and isolated elongated processes. Total volumes ranged from 29,258 to 263,762 µm^3, with a mean of 114,774 ± 5,809 (Fig. 1D). The values are substantially larger than those reported in rat (Bushong et al., 2002) and mouse hippocampus (Ogata and Kosaka, 2002) and cortex (Halassa et al., 2007; Grosche et al., 2013), but smaller than have been reported for human cortical astrocytes (Oberheim et al., 2009).

To be confident that the larger measured volume of ferret astrocytes was not a function of differences in methodology, we repeated our measurements in astrocytes electroporated in mouse visual cortex. We found that mouse astrocytes had an average volume of 64,831 ± 4314 (range 43,350–94,166; Fig. 1C), which confirms that astrocytes in ferret visual cortex are approximately two times larger than in mouse (Fig. 1D). Mouse astrocytes further had more homotypic morphologies, and were more spherical, with fewer invaginations and isolated processes than in the ferret population.

This result suggested that, in order for the tiling arrangement to apply, there would need to be significantly lower density of astrocytes in ferret visual cortex. To address this possibility, we next characterized the spatial distribution of astrocyte somata in ferrets and mice with regard to the lamination pattern of neuronal cell bodies in visual cortex. We identified astrocyte and neuronal somata in 50-µm fixed tissue sections immunostained for S100 and NeuN, respectively (Fig. 2A). Clear laminar differences in neuronal density enabled us to automatically delineate the cortical layers (Fig. 2B,C). Interestingly, astrocyte density was relatively constant across cortical layers (Fig. 2D). The analysis of the density of astrocytes across all layers revealed that there were 2.48 ± 0.15 neurons for every astrocyte in ferrets (17,896 ± 952 astrocytes/mm^3). If astrocytes tile visual cortex, as they do in mouse hippocampus, then each astrocyte will correspond to a volume of 55,879 ± 3,078 µm^3. This value is noteworthy, because it is much smaller than our measured value for the average volume of ferret astrocyte territory, suggesting that there is more overlap of processes from neighboring astrocytes in ferret than previously reported in rodent.

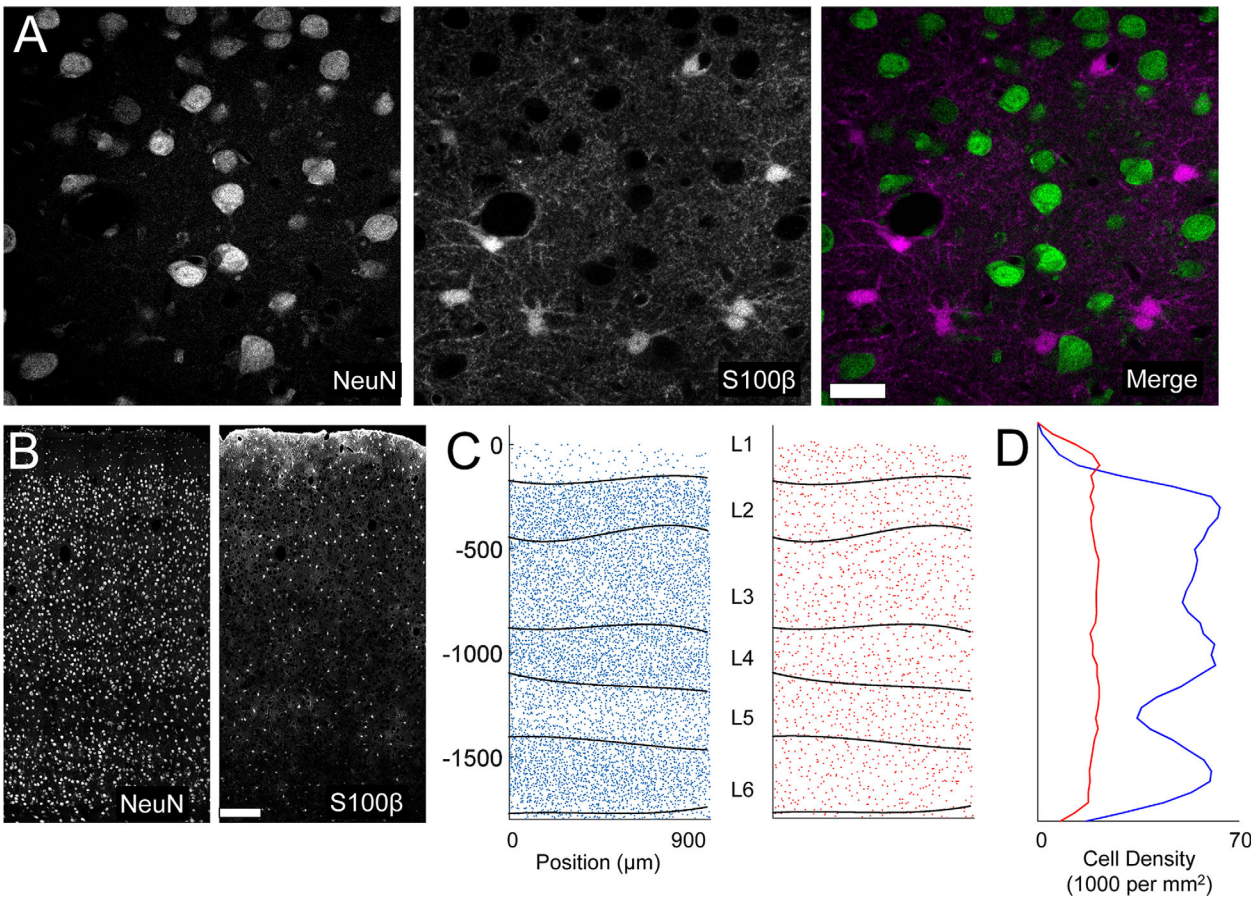

Figure 2. Spatial distribution of astrocyte somata. **A:** High-magnification example of double staining for NeuN (left) and S100 (right). **B:** Example of mosaic images for NeuN and S100 through all cortical layers. **C:** Example of the cell body locations obtained from the same z-stack as images in B. The automatically defined layer boundaries (L1–L6) are overlaid on each plot. **D:** Plot of cell density as a function of cortical depth computed from the data in C. Scale bar = 20 μm in A; 200 μm in B.

Given the large range of territory sizes and shapes of ferret astrocytes, we wanted to evaluate whether there was a relationship between the arrangement of astrocyte soma locations and territory shape and size. An analysis of nearest neighbor astrocyte distances differed markedly from a random distribution of cell locations in two notable ways (Fig. 3A). The most prominent peak in the distribution of nearest neighbors was at 30 μm, which is substantially larger than expected for randomly distributed (22 μm). The second peak of nearest neighbors represents cell that are less than 12 μm apart.

High-resolution confocal images of these cell pairs revealed that they had cell bodies that were essentially touching, and we refer to these cells as "kissing" pairs (Fig. 3B). These pairs have been noted previously, dating back to Ramón y Cajal (1899), but studies of their prevalence and features are scarce. At the resolution afforded by confocal imaging, even the nuclei of these cells appear to be touching (Fig. 3C). Immunostaining for the major astrocyte gap-junction protein connexin43 (Cx43) demonstrated that all such kissing pairs had dense Cx43 expression on the touching membrane segments (Fig. 3C). This is consistent with the strong electrical coupling measured between closely spaced astrocyte pairs in the hippocampus (Xu et al., 2010, 2014).

Spatial analysis of kissing pair locations showed that they are not uniformly distributed through the cortex; the proportion was much higher in cortical layers 3 and 4 (Fig. 3D). In these layers, more than 20% of astrocytes are found in a kissing pair, whereas in layer 2, only ~10% were. Layer 4 and deep layer 3 are the primary targets of afferent projections from the lateral geniculate nucleus (Humphrey et al., 1985; Erisir and Dreusicke, 2005; Nahmani and Erisir, 2005). We stained for VGlut2 to identify thalamocortical terminals, and compared the spatial distribution of these terminals with the distribution of kissing pairs (Fig. 3D, right). We found a close relationship between the two, suggesting

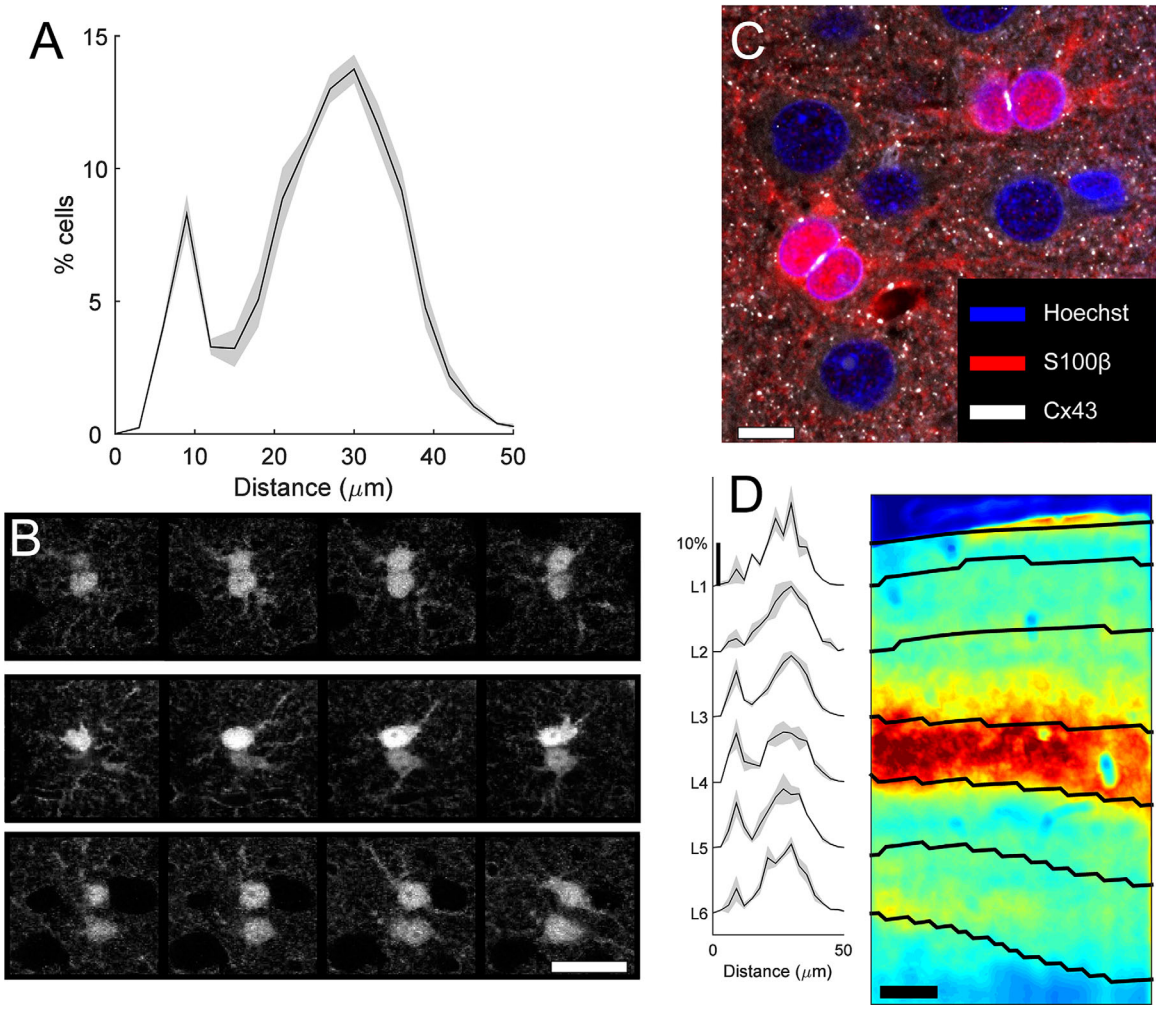

Figure 3. Spatial distribution of astrocyte nearest neighbors. **A:** Histogram of nearest neighbor distances (mean [line] ± SEM [gray shadow]). **B:** Examples of two pairs of kissing cells (top two rows), and one non-kissing cell pair (bottom row) stained for S100. Each row contains four images from a z-stack, separated by 2 μm. **C:** Confocal image of triple-stained tissue (Hoechst, blue; S100, red; Cx43, white) showing close apposition of kissing astrocytes. **D:** Histogram of nearest neighbor distances for cells located in each cortical layer (mean [line] ± SEM [gray shadow]). Image on right is immunostained for VGlut2. The image was low-pass filtered and clipped at 0.5% pixels for display. Scale bar = 200 μm in B–D.

that kissing astrocytes may be related to the different synaptic organization in these layers.

It was previously shown that these cells could be astrocytes undergoing proliferation (Ge et al., 2012; Bardehle et al., 2013); however, these cells were immunonegative for markers of cells in division (Ki67), and were also not detectable by bromodeoxyuridine (BrdU) staining following either brief or prolonged BrdU treatment (data not shown), suggesting that they are not dividing cells. Consistent with this conclusion, Nimmerjahn et al. (2004) reported long-term stability of SR101-stained astrocytes, including closely spaced pairs within 15 μm of each other.

These results demonstrated that there is substantial heterogeneity in territory shape, size, and spacing of somata in ferret astrocytes. This raised the question of whether there is a relationship between the shape of an astrocyte territory and the distance to its neighbors. To address this, we targeted electroporations with two spectrally distinct fluorescent molecules to pairs (or larger groups) of adjacent astrocytes (Fig. 4A). We collected z-stack image series from 39 such pairs, and analyzed the overlap of processes of reconstructed territories. Consistent with our analysis of the density and size of astrocyte territories, we observed that many pairs of neighboring astrocytes indeed had a large overlap of their processes (Fig. 4B). There was a large range of overlap, ranging from 0% up to 50% of territory volume. Because soma locations are nonrandomly arranged, we asked whether there were any specific

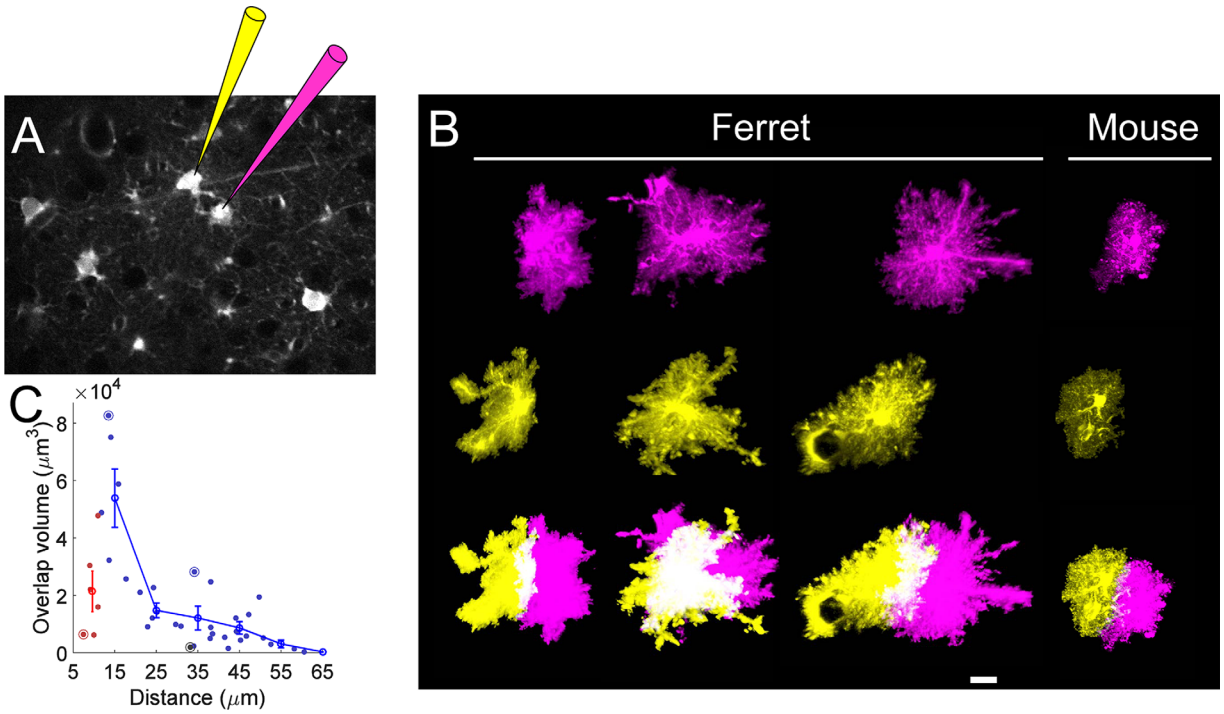

Figure 4. Measurement of volume of territory overlap. **A:** Schematic showing dual electroporation of adjacent SR101-positive astrocytes with two spectrally distinct fluorophores. **B:** Three examples of territory overlap from reconstructed pairs of neighbors. The right-most pair is from mouse. Top two rows show a projection of the reconstructed surface rendering of each cell in the pair. Bottom row shows the overlay of the two cells, in which the images have been saturated to emphasize the color distinction of the region of overlap (white). **C:** Plot of overlap volume as a function of distance between somas. Scatterplot shows measurements from kissing cell pairs (red) and non-kissing cells (blue). The mean (line) ± SEM (gray shadow) for bins of width 10 μm is overlaid. Circles indicate the cells shown in B. Scale bar = 20 μm in B.

rules governing the relationship between the territory morphology of an astrocyte and the arrangement of nearby astrocytes surrounding it.

We analyzed the amount of overlap between adjacent pairs as a function of somatic distance (Fig. 4C). There was a strong negative relationship between intersoma distance and amount of overlap for cell pairs separated by 15–55 μm. Interestingly, that rule did not apply for kissing cell pairs (separated by less than ~12 μm), many of which had very little overlap. The break from this relationship in the kissing pairs ($n = 5$) shows that these cells follow different rules for interaction of their processes, and suggests that they may be a distinct class of astrocyte.

In the hippocampus, astrocyte morphology, size, and territory overlap are developmentally regulated over the time period of synaptogenesis (Bushong et al., 2004). The age of the ferrets in our sample (P60–P80) was chosen to represent mature astrocytes. At this age, the critical period has closed, and synaptic refinement is generally complete (Issa et al., 1999; Huberman et al., 2008). Nevertheless, due to the surprising amount of overlap observed, we decided to measure astrocyte size and overlap in astrocytes from fully mature adults (1 year old), to eliminate any possibility of a developmental phenomenon. The distribution of territory volumes were not statistically different between the two age groups (Fig. 5A; $p = 0.24$ by Student's t-test). In addition, the relationship between territory overlap and distance was very similar (Fig. 5B). The results from the older population confirm the conclusion that mature astrocytes in ferret visual cortex are larger and morphologically more heterogeneous, and share more territory with their neighbors than in rodents.

The preceding analysis suggested that the standard tiling model may be too simple to capture the arrangement of astrocyte somata and processes in ferret visual cortex. To build a more realistic description of the relationship between soma spacing and territory overlap, we incorporated our measurements into a simple model that enabled us to simulate alternative rules that could govern the arrangement of astrocytes. We first fit an exponential curve to the distance versus overlap data from non-kissing astrocyte pairs (Fig. 6A). We then used this curve to predict the overlap of each cell pair in the S100-stained tissue (within a 55-μm

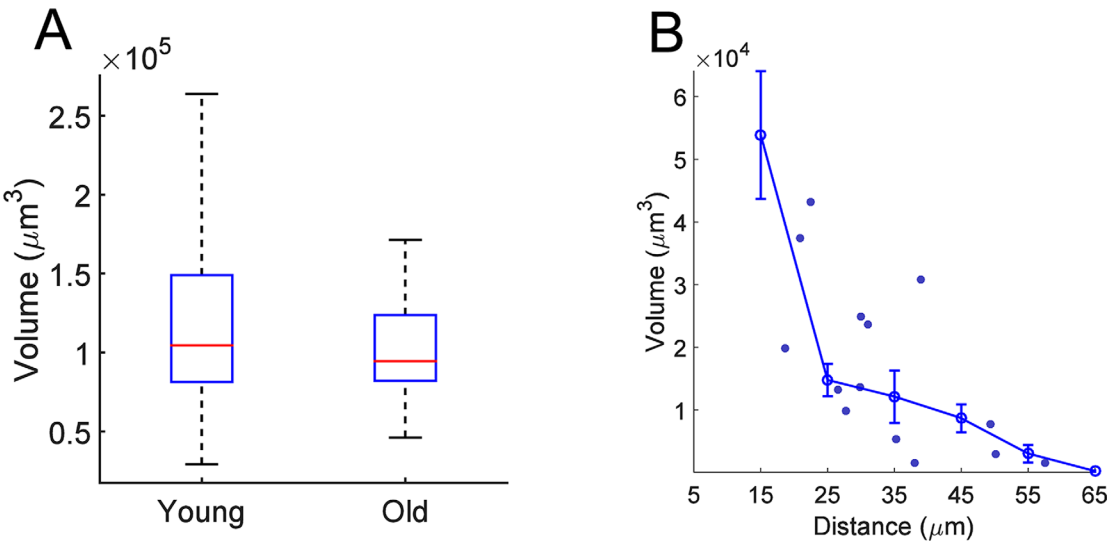

Figure 5. Measurement of overlap volume in older ferrets. **A:** Boxplot showing comparison of territory volumes between young adult ferrets (replotted from Fig. 1D) and old ferrets. Boxplots represent the median and interquartile range (25th and 75th percentile), and whiskers represent the minimum and maximum values. **B:** Comparison of overlap volume versus distance between young adult ferrets and old ferrets. Individual points are measurements from older ferrets. Error bar shows binned averages (line) ± SEM (gray shadow), replotted from Figure 4C.

neighborhood). On average, there were 7.85 ± 0.03 astrocytes within this neighborhood (Fig. 6B). This enabled us to predict the overlap of each astrocyte with all other neighboring astrocytes, as illustrated in Figure 6C. In this example, there are four neighboring cells. For each of these, the shared (overlapping) volume was predicted from the curve, and the total shared volume was produced by adding these values.

We then applied this method to each cell in our population of S100-stained cells. As expected, there was a strong relationship between the number of neighbors and the total predicted shared volume (Fig. 6D). However, there was also a very broad distribution of predicted shared volume, regardless of the number of neighbors. This is largely a function of the non-uniform spacing of astrocytes in the tissue. The predicted shared volume was then compared with the average volume of the territories (Fig. 1D) to compute the predicted exclusive territory, which is the percentage of territory that does not overlap with any neighbors. The mean value across all astrocytes in all cortical layers was 49.4% (range 46.9–51.7 across layers). Interestingly, the distribution of predicted exclusive territory values (Fig. 6E) showed a large range, from zero (no exclusive territory) to 100 (no overlap with any neighbors). As expected from the ratio of measured astrocyte volumes and volume available per astrocyte, this model predicted that, on average, half of cortical tissue is covered by processes from multiple astrocytes. However, the broad range of predicted exclusive territory raised the question of whether territory shapes are influenced by the shapes of their neighbors, or are intrinsically or randomly determined.

To distinguish between these possibilities, we ran another simulation. We generated spheres that matched the volumes measured in our sample (Fig. 7A), and we then placed these spheres randomly, at the true locations of astrocytes, and measured the overlap volume with all touching neighbors from this simulation. This simulates the case in which the particular shape of an astrocyte is not influenced by the location or shape of its neighbors. When we compared the relationship between this simulated overlap and distance with the fit to our data, there was a striking difference (Fig. 7B). The measured overlap was substantially less than in the simulated spherical case. In fact, the curve derived from the data closely matches the lower bound on the distribution from the simulation. This suggests that astrocytes have a morphology that in fact minimizes the overlap of their processes, given the constraints of their size and their spacing.

DISCUSSION

We have assessed the spatial arrangement, morphology, and territory overlap of astrocytes in mice and ferret visual cortex. We have identified two major features suggesting that standard models may need to be expanded to encompass the astrocyte diversity in different brain regions and species. First, we found that

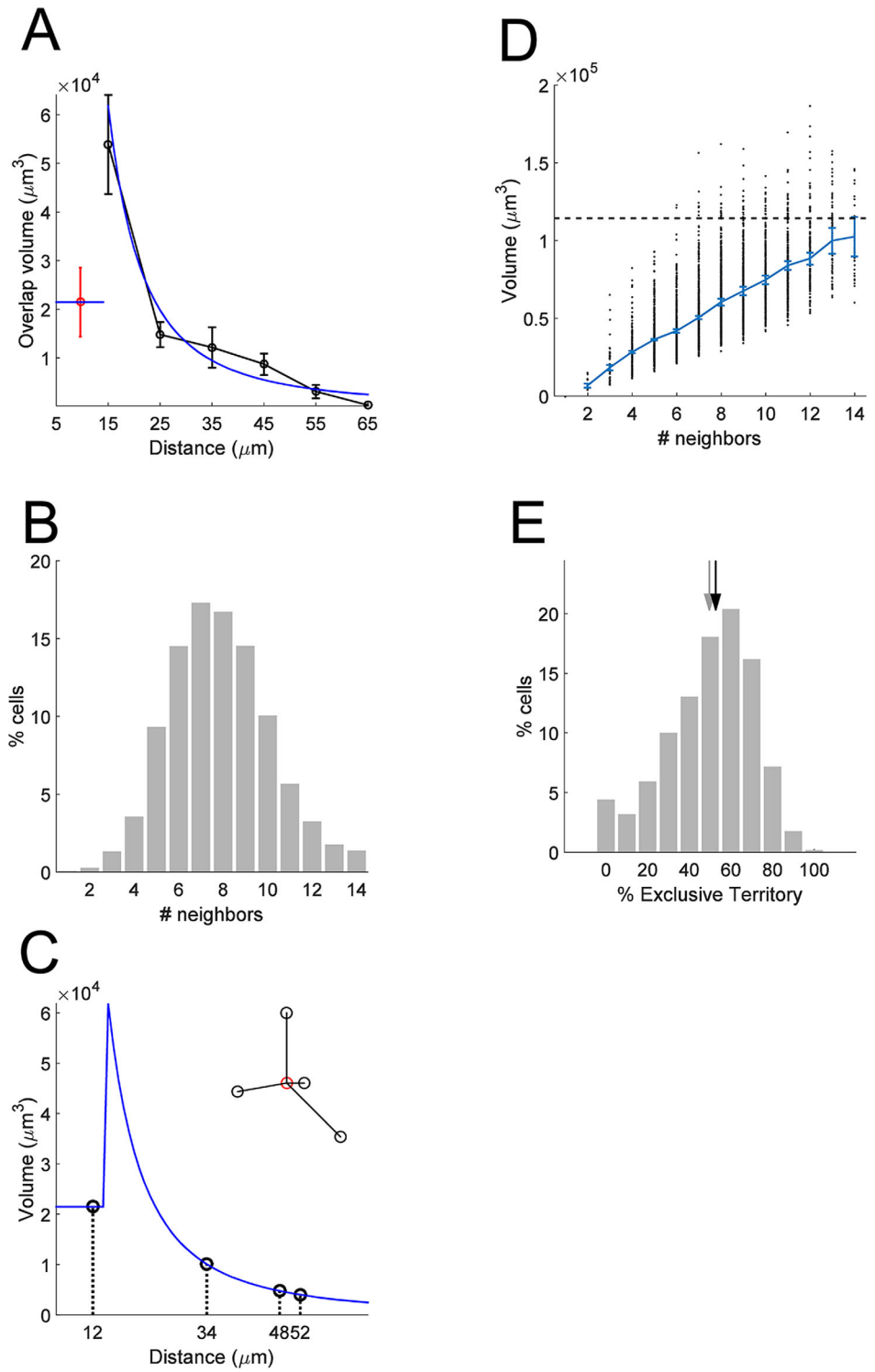

Figure 6. Estimate of the exclusive territory. **A:** The relationship between overlap and distance is modeled by an exponential curve fit to the data for non-kissing cell pairs. The black curve is the means of the data from Figure 4C. The blue curve is the exponential fit. Values below 15 μm are assumed to have constant value of the mean for the kissing pairs. **B:** A schematic example of use of the model to estimate total overlapping volume for an astrocyte, with all touching neighbors. The inset shows the spatial arrangement of an astrocyte and four neighbors. The volume of overlap is computed from the value of the exponential model taken at the distance for each pair. **C:** Cumulative distribution plot of the number of touching pairs (less than 55-μm separation) across the population of S100-positive cells. **D:** Scatterplot of the total overlap volume computed by the model for each S100-positive astrocyte, as a function of the number of neighboring cells. The mean (± SEM) is overlaid. Dashed line represents the mean volume of all electroporated astrocytes, for comparison. **E:** Histogram of the estimated exclusive territory for all astrocytes. Black and gray arrows demarcate mean and median.

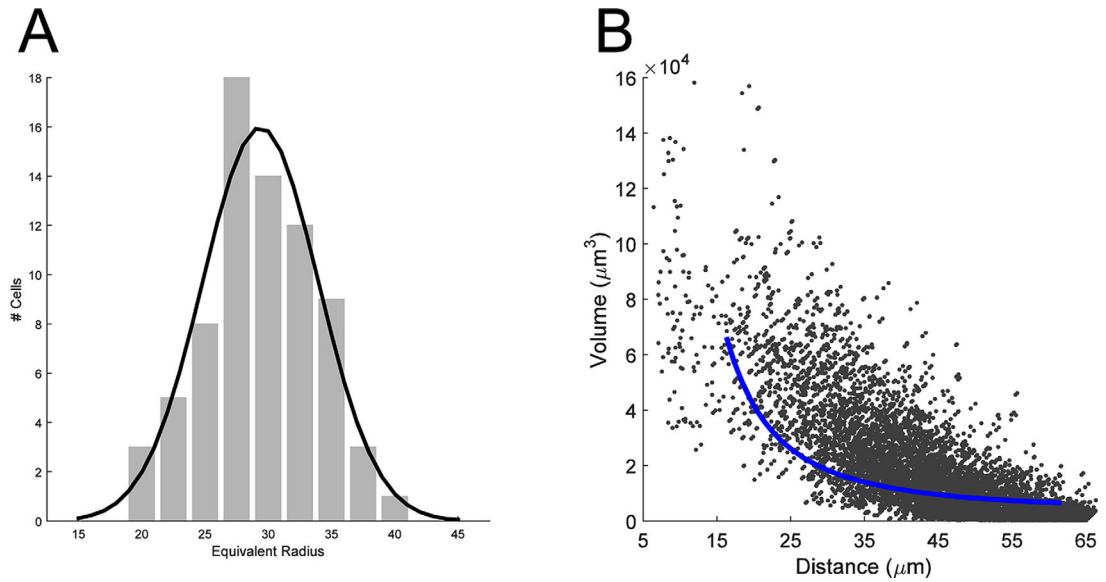

Figure 7. Model of spherical territories. **A:** The distribution of the equivalent radius for the population of astrocytes (gray bars). Black line is the gaussian fit used to generate the spherical territories in the model. **B:** Plot of the simulated volume of overlap, as a function of distance. Blue line represents the exponential fit to the original data, replotted from Figure 6A.

there is substantially more overlap of the processes of neighboring ferret cortical astrocytes than in rodents, suggesting that the tiling model, in which astrocytes exclusively invest neural tissue, may not apply in ferret visual cortex. We estimate that at most 50% of ferret cortical tissue is covered by a single astrocyte. Second, we observed that pairs of astrocytes with directly contacting cell bodies expressing connexin 43 (kissing astrocytes) do not follow the same rules governing the overlap of their processes. Furthermore, these cells are particularly prevalent in the thalamo-recipient layers of cortex, in which neurons have distinct functional receptive field properties, which suggests that these cells may constitute a distinct class of astrocyte. These results contribute to the emerging awareness of astrocyte diversity and circuit specificity.

Territory overlap and tiling

Since the studies of Bushong et al. (2002) and Ogata and Kosaka (2002), the notion that astrocytes tile neural tissue with minimally overlapping territories has become the standard model for astrocyte organization. In spite of growing attention to astrocyte heterogeneity (Oberheim et al., 2006; Matyash and Kettenmann, 2010; Khakh and Sofroniew, 2015), few studies have made direct, quantitative measurements of territory volume and overlap in other brain regions or species. In fact, there are examples of differences among brain regions and species. The processes of Bergmann glia in the cerebellum overlap substantially (Grosche et al., 2002), suggesting that territory overlap may relate to the functional requirements of particular neural circuits. Human cortical astrocytes also overlap more than rodent ones (Oberheim et al., 2009). Our results provide additional evidence that caution should be used in making generalizations about astrocyte morphology and organization in different brain regions or species.

Differences in the morphology and organization of astrocytes between mice and ferrets could be related to a number of factors, including the gyrencephalic versus lissencephalic brains, or the columnar organization of visual cortex, which is absent in rodent cortex (Ohki and Reid, 2007; Van Hooser, 2007). It can be explained as a result of either intrinsic differences in the astrocyte, or as a result of plastic changes due to environmental factors. Supporting the first notion, it was recently shown that human astrocytes transplanted into mouse cerebral cortex functionally incorporated into the neuronal circuit and expressed characteristic size, shape, and volume of human astrocytes despite the murine neural environment (Han et al., 2013; Goldman et al., 2015). There is also evidence that astrocyte morphology can be dynamically altered by external factors, such as neural activity levels. One exquisite example of this occurs in physiological conditions within the supraoptic nucleus of the hypothalamus, where astrocytes extend and retract their processes in response to changes in neuronal activity related to lactation (Piet et al., 2002; Theodosis et al., 2006). In the same way, astrocyte size and complexity is influenced by housing

TABLE 1.
Antibodies Used in This Study

Antigen	Immunogen	Source, host species, cat. #, clone or lot #,	RRID	Dilution
S100	Recombinant full-length protein (cow).	Rabbit polyclonal; Abcam, cat. # ab868;	AB Registry ID: AB_306716	1:500
NeuN	Purified cell nuclei from mouse brain	Mouse monoclonal; Millipore, cat. # MAB377;	AB Registry ID: AB_2298772	1:5,000
VGlut2	Final 18 amino acids of the C-terminal of rat VGLUT-2	Guinea pig; Millipore, cat. # AB2251	AB Registry ID: AB_1587626	1:5,000
Connexin 43	Rat connexin-43 amino acids 252–270	Mouse monoclonal; BD Biosciences, cat# 610061	AB Registry ID: AB_397473	1:5,000

conditions: animals that are reared in socially stimulating and enriched environments have an increase in mean size and number of astrocytes (Sirevaag and Greenough, 1991) and a delay in maturation when sensory activity is decreased, as happens in monocular deprivation in rats and cats (Muller, 1990; Hawrylak and Greenough, 1995). This is noteworthy, because ferrets are most often reared in more socially stimulating environments (like the ones used in this study) in comparison with mice.

The molecular mechanisms involved in astrocyte spacing and territory overlap are poorly understood. Recent studies of astrocytes in *Drosophila* suggest that the extent of astrocyte territories is determined by a balance between repulsive interactions with neighboring astrocytes and the promotion of growth and elaboration of astrocytic process by neuronal release of fibroblast growth factor (FGF) ligands. The balance between repulsive and growth factors determines the size of the astrocyte territory (Stork et al., 2014). If similar factors interact in mammalian cortex, a parsimonious explanation for our results could be that astrocytes in ferret visual cortex experience an environment with a higher ratio of neuronally derived growth-promoting factors to astrocyte-derived repulsive factors, compared with mouse astrocytes.

The functional consequences of overlapping territories have not been established. Several groups (Bushong et al., 2003, 2004; Halassa et al., 2007) have speculated that the single-astrocyte territories endow each astrocyte with exclusive regulatory control over the synapses within their territory, estimated to be ~140,000 for a typically sized astrocyte in area CA1 of the hippocampus (Bushong et al., 2002). Such an arrangement would enable a spatial scale of regulation distinct from both the point-to-point synaptic regulation and the volume diffusion neuromodulatory regulation. Whether such territory-delimited regulatory influence has a distinct functional role will require further study.

Our results predict that ~50% of cortical tissue in ferret is covered by more than one astrocyte. For multiple reasons, this is likely to be an underestimate. First, territory volume measurements depend critically on the intracellular distribution of the marker. Soluble cytosolic markers have been found to underestimate astrocyte volume compared with membrane-bound markers, due to the extremely small volume-to-surface area ratio in the most peripheral processes (Haustein et al., 2014). Second, the number of touching neighbors that we include in our model is almost certainly an underestimate, due to edge-effects resulting from finite (50-μm) tissue sections. For simplicity, we chose not to attempt to correct for these effects, although they can be substantial (e.g., half of the neighbors are excluded for cells at the bottom or top of the slice). Third, we observed several examples in which the processes of an astrocyte surrounded the soma of its neighbor. We also noted several examples in which the processes of two astrocytes overlapped (or nearly overlapped) despite the presence of a third astrocyte in between them. All of these factors together strongly indicate that our estimates of exclusive territory are likely to be a significant overestimate.

Our strategy for in vivo filling of astrocytes by SR101 targeting is novel, and potential differences with previous methods warrants discussion. The advantages of our approach represent a trade-off with potential confounds of exogenous application of SR101 and electroporation. Labeling astrocytes with SR101 enabled us to preselect the astrocytes to fill, which was important to select pairs at specific distances, and with classic astrocytic morphology (excluding oligodendrocytes, for example, which have also been suggested to be labeled by SR101). Furthermore, our strategy enabled us to take measurements in vivo, which eliminates potential artifacts arising from slice preparations, including effects of fixation, hypoxia, and changes in ionic or osmotic balance, all of which are critical for astrocyte morphology (Stokum et al., 2016). Potential concerns

with our approach arise from the reported epileptogenic effects of SR101 (Kang et al., 2010), or damage related to electroporation, which might theoretically alter astrocyte morphology on the rapid timescale of our experiments. These concerns are largely alleviated by the interspecies control: the clear differences seen between ferret and mouse astrocytes, despite the identical labeling and filling procedures in both species.

Laminar differences in astrocyte organization

We have found that there is a dramatically higher proportion of kissing astrocytes in thalamo-recipient layers 3–4 of ferret visual cortex. These layers have several distinct properties, which are related to the fact that all inputs to cortex are gated through the activity in these layers. Thalamo-cortical synapses are generally of the "driver" type, which are structurally and functionally distinct from intracortical "modulator" synapses (Sherman and Guillery, 1998). Receptive fields in these layers are more linear, "simple cells," which therefore are more active during natural vision conditions (Usrey et al., 2003). Cytochrome oxidase activity is highest in thalamo-recipient layers (Innocenti et al., 2002), suggesting that there is a higher metabolic demand in these layers. Consistent with this, there is a peak in the density of vasculature in layer 4 in both rodent barrel cortex and macaque visual cortex (Weber et al., 2008; Blinder et al., 2013). Thus, it is likely that kissing pairs are related to different demands of functionally distinct cortical compartments, but further study will be required to determine which aspect of astrocyte function is advantageous to meet the needs in these layers.

Kissing astrocytes have been observed, going back to Ramón y Cajal (1899); however, their prevalence and arrangement have not been well characterized. Nimmerjahn et al. (2004) noted a population of astrocytes in rat and mouse cortex that were located in very close proximity, but did not appear to be directly touching. Bardehle et al. (2013) state that they only observed such cell pairs in mouse cortex subsequent to injury-induced proliferation. Ge et al. (2012) observed live cell divisions that gave rise to transient kissing pairs during early development, but not in adult (P50) mouse tissue. Further study will be necessary to identify the prevalence of these cells in different neural tissue compartments, and in different species.

Functional implications

It is noteworthy that astrocyte calcium signals have been reported to differ somewhat between studies in ferret and mouse visual cortex (Schummers et al., 2008; Bonder and McCarthy, 2014; Paukert et al., 2014). In mouse cortex, activity-driven calcium events in individual astrocytes are relatively rare, whereas synchronized events among neighboring astrocytes are much more prominent (Paukert et al., 2014). This difference with ferret astrocyte behavior may reflect different states of anesthesia (Schummers et al., 2008; Thrane et al., 2012), species differences in astrocyte organization such as we describe here, or differences in neural activity patterns between species. It is also possible that the latter two factors are inter-related; increased coordinated activity during epilepsy has been reported to lead to increased overlap between the processes of neighboring astrocytes (Oberheim et al., 2008). It is therefore conceivable that the degree of astrocyte territory overlap is closely related to levels of synchronized activity, which is higher in ferret visual cortex than mouse, owing to the columnar organization and higher firing rates.

Although ferret astrocytes express connexin proteins, calcium responses in layer 2 astrocytes are independent of their neighbors (Schummers et al., 2008). This raises the question of when, and to what extent, astrocytes in ferret visual cortex act as independent units instead of as a syncytium. Astrocyte network communication through gap junctions is also essential for the correct distribution of potassium, glutamate, and water (Pannasch et al., 2011). Astrocytes not gap-junction–coupled to their neighbors are still able to take up ions and metabolites but fail to distribute them through the network.

Based on these notions, it is possible that the size of ferret astrocytes is a compensation, to balance network connectivity for metabolic purposes with independent calcium signaling capability. The idea that astrocytes are acting as independent units has benefits regarding the fine scale at which bidirectional communication between astrocytes and neurons would occur. However, in a model with no overlap plus no functional connections, the events occurring in one territory would be isolated and would have little influence over their neighbors. In this sense, the fact that ferret astrocytes share 50% of their domain with their neighbors would let other neurons and astrocytes know what is happening in the neighborhood. The inverse relationship between the presence of gap junctions and overlap matches our data regarding kissing pairs, in which the gap coupling, not overlap, is preserved. The data presented here point to a new form of astrocyte organization with the purpose of preserving local independent bidirectional communication with neurons and an astrocytic network connected mainly through the neuropil shared between neighbor astrocytes.

ACKNOWLEDGMENTS

We are grateful to Andrew Li for assistance with confocal imaging and data preprocessing, and to Kirill Safin for his contributions to software routines. We are grateful to the MPFI Molecular Core Facility for assistance with western blots and antibody characterization.

ROLE OF AUTHORS

All authors had full access to all the data in the study and take full responsibility for the integrity of the data and the accuracy of the data analysis. MLH performed the experiments, analyzed the data, and wrote the manuscript. WH performed immunohistology, and provided surgical assistance. JMS performed analysis and wrote the manuscript.

CONFLICT OF INTEREST STATEMENT

The authors declare they have no competing financial interests.

LITERATURE CITED

Agulhon C, Fiacco TA, McCarthy KD. 2010. Hippocampal short- and long-term plasticity are not modulated by astrocyte Ca2+ signaling. Science 327:1250–1254.

Araque A, Carmignoto G, Haydon PG, Oliet SH, Robitaille R, Volterra A. 2014. Gliotransmitters travel in time and space. Neuron 81:728–739.

Attwell D, Buchan AM, Charpak S, Lauritzen M, Macvicar BA, Newman EA. 2010. Glial and neuronal control of brain blood flow. Nature 468:232–243.

Bardehle S, Kruger M, Buggenthin F, Schwausch J, Ninkovic J, Clevers H, Snippert HJ, Theis FJ, Meyer-Luehmann M, Bechmann I, Dimou L, Gotz M. 2013. Live imaging of astrocyte responses to acute injury reveals selective juxtavascular proliferation. Nat Neurosci 16:580–586.

Blinder P, Tsai PS, Kaufhold JP, Knutsen PM, Suhl H, Kleinfeld D. 2013. The cortical angiome: an interconnected vascular network with noncolumnar patterns of blood flow. Nat Neurosci 16:889–897.

Bonder DE, McCarthy KD. 2014. Astrocytic Gq-GPCR-linked IP3R-dependent Ca2+ signaling does not mediate neurovascular coupling in mouse visual cortex in vivo. J Neurosci 34:13139–13150.

Bushong EA, Martone ME, Jones YZ, Ellisman MH. 2002. Protoplasmic astrocytes in CA1 stratum radiatum occupy separate anatomical domains. J Neurosci 22:183–192.

Bushong EA, Martone ME, Ellisman MH. 2003. Examination of the relationship between astrocyte morphology and laminar boundaries in the molecular layer of adult dentate gyrus. J Comp Neurol 462:241–251.

Bushong EA, Martone ME, Ellisman MH. 2004. Maturation of astrocyte morphology and the establishment of astrocyte domains during postnatal hippocampal development. Int J Dev Neurosci 22:73–86.

Chapman B, Stryker MP. 1993. Development of orientation selectivity in ferret visual cortex and effects of deprivation. J Neurosci 13:5251–5262.

Clarke LE, Barres BA. 2013. Emerging roles of astrocytes in neural circuit development. Nat Rev Neurosci 14:311–321.

Erisir A, Dreusicke M. 2005. Quantitative morphology and postsynaptic targets of thalamocortical axons in critical period and adult ferret visual cortex. J Comp Neurol 485: 11–31.

Filosa JA, Morrison HW, Iddings JA, Du W, Kim KJ. 2015. Beyond neurovascular coupling, role of astrocytes in the regulation of vascular tone. Neuroscience 323:96–109.

Ge WP, Miyawaki A, Gage FH, Jan YN, Jan LY. 2012. Local generation of glia is a major astrocyte source in postnatal cortex. Nature 484:376–380.

Goldman SA, Nedergaard M, Windrem MS. 2015. Modeling cognition and disease using human glial chimeric mice. Glia 63:1483–1493.

Granot I, Dekel N. 1994. Phosphorylation and expression of connexin-43 ovarian gap junction protein are regulated by luteinizing hormone. J Biol Chem 269:30502–30509.

Grosche A, Grosche J, Tackenberg M, Scheller D, Gerstner G, Gumprecht A, Pannicke T, Hirrlinger PG, Wilhelmsson U, Huttmann K, Hartig W, Steinhauser C, Pekny M, Reichenbach A. 2013. Versatile and simple approach to determine astrocyte territories in mouse neocortex and hippocampus. PLoS One 8:e69143.

Grosche J, Kettenmann H, Reichenbach A. 2002. Bergmann glial cells form distinct morphological structures to interact with cerebellar neurons. J Neurosci Res 68:138–149.

Halassa MM, Fellin T, Takano H, Dong JH, Haydon PG. 2007. Synaptic islands defined by the territory of a single astrocyte. J Neurosci 27:6473–6477.

Han X, Chen M, Wang F, Windrem M, Wang S, Shanz S, Xu Q, Oberheim NA, Bekar L, Betstadt S, Silva AJ, Takano T, Goldman SA, Nedergaard M. 2013. Forebrain engraftment by human glial progenitor cells enhances synaptic plasticity and learning in adult mice. Cell Stem Cell 12:342–353.

Haustein MD, Kracun S, Lu XH, Shih T, Jackson-Weaver O, Tong X, Xu J, Yang XW, O'Dell TJ, Marvin JS, Ellisman MH, Bushong EA, Looger LL, Khakh BS. 2014. Conditions and constraints for astrocyte calcium signaling in the hippocampal mossy fiber pathway. Neuron 82:413–429.

Hawrylak N, Greenough WT. 1995. Monocular deprivation alters the morphology of glial fibrillary acidic protein-immunoreactive astrocytes in the rat visual cortex. Brain Res 683:187–199.

Henneberger C, Bard L, King C, Jennings A, Rusakov DA. 2013. NMDA receptor activation: two targets for two coagonists. Neurochem Res 38:1156–1162.

Huberman AD, Feller MB, Chapman B. 2008. Mechanisms underlying development of visual maps and receptive fields. Annu Rev Neurosci 31:479–509.

Humphrey AL, Sur M, Uhlrich DJ, Sherman SM. 1985. Projection patterns of individual X- and Y-cell axons from the lateral geniculate nucleus to cortical area 17 in the cat. J Comp Neurol 233:159–189.

Innocenti GM, Manger PR, Masiello I, Colin I, Tettoni L. 2002. Architecture and callosal connections of visual areas 17, 18, 19 and 21 in the ferret (*Mustela putorius*). Cereb Cortex 12:411–422.

Issa NP, Trachtenberg JT, Chapman B, Zahs KR, Stryker MP. 1999. The critical period for ocular dominance plasticity in the ferret's visual cortex. J Neurosci 19:6965–6978.

Jourdain P, Bergersen LH, Bhaukaurally K, Bezzi P, Santello M, Domercq M, Matute C, Tonello F, Gundersen V, Volterra A. 2007. Glutamate exocytosis from astrocytes controls synaptic strength. Nat Neurosci 10:331–339.

Kang J, Kang N, Yu Y, Zhang J, Petersen N, Tian GF, Nedergaard M. 2010. Sulforhodamine 101 induces long-term potentiation of intrinsic excitability and synaptic efficacy in hippocampal CA1 pyramidal neurons. Neuroscience 1691601–1609.

Khakh BS, Sofroniew MV. 2015. Diversity of astrocyte functions and phenotypes in neural circuits. Nat Neurosci 18:942–952.

Kim KJ, Iddings JA, Stern JE, Blanco VM, Croom D, Kirov SA, Filosa JA. 2015. Astrocyte contributions to flow/pressure-evoked parenchymal arteriole vasoconstriction. J Neurosci 35:8245–8257.

Koster-Patzlaff C, Hosseini SM, Reuss B. 2008. Layer specific changes of astroglial gap junctions in the rat cerebellar cortex by persistent Borna Disease Virus infection. Brain Res 1219:143–158.

Matyash V, Kettenmann H. 2010. Heterogeneity in astrocyte morphology and physiology. Brain Res Rev 63:2–10.

Mei X, Ezan P, Giaume C, Koulakoff A. 2010. Astroglial connexin immunoreactivity is specifically altered at beta-amyloid plaques in beta-amyloid precursor protein/presenilin1 mice. Neuroscience 171:92–105.

Molofsky AV, Krencik R, Ullian EM, Tsai HH, Deneen B, Richardson WD, Barres BA, Rowitch DH. 2012. Astrocytes and disease: a neurodevelopmental perspective. Genes Dev 26:891–907.

Muller CM. 1990. Dark-rearing retards the maturation of astrocytes in restricted layers of cat visual cortex. Glia 3:487–494.

Murphy-Royal C, Dupuis JP, Varela JA, Panatier A, Pinson B, Baufreton J, Groc L, Oliet SH. 2015. Surface diffusion of astrocytic glutamate transporters shapes synaptic transmission. Nat Neurosci 18:219–226.

Nahmani M, Erisir A. 2005. VGluT2 immunochemistry identifies thalamocortical terminals in layer 4 of adult and developing visual cortex. J Comp Neurol 484:458–473.

Nimmerjahn A, Kirchhoff F, Kerr JN, Helmchen F. 2004. Sulforhodamine 101 as a specific marker of astroglia in the neocortex in vivo. Nat Methods 1:31–37.

Oberheim NA, Wang X, Goldman S, Nedergaard M. 2006. Astrocytic complexity distinguishes the human brain. Trends Neurosci 29:547–553.

Oberheim NA, Tian GF, Han X, Peng W, Takano T, Ransom B, Nedergaard M. 2008. Loss of astrocytic domain organization in the epileptic brain. J Neurosci 28:3264–3276.

Oberheim NA, Takano T, Han X, He W, Lin JH, Wang F, Xu Q, Wyatt JD, Pilcher W, Ojemann JG, Ransom BR, Goldman SA, Nedergaard M. 2009. Uniquely hominid features of adult human astrocytes. J Neurosci 29:3276–3287.

Ogata K, Kosaka T. 2002. Structural and quantitative analysis of astrocytes in the mouse hippocampus. Neuroscience 113:221–233.

Ohki K, Reid RC. 2007. Specificity and randomness in the visual cortex. Curr Opin Neurobiol 17:401–407.

Otsu Y, Couchman K, Lyons DG, Collot M, Agarwal A, Mallet JM, Pfrieger FW, Bergles DE, Charpak S. 2015. Calcium dynamics in astrocyte processes during neurovascular coupling. Nat Neurosci 18:210–218.

Pannasch U, Vargova L, Reingruber J, Ezan P, Holcman D, Giaume C, Sykova E, Rouach N. 2011. Astroglial networks scale synaptic activity and plasticity. Proc Natl Acad Sci U S A 108:8467–8472.

Paukert M, Agarwal A, Cha J, Doze VA, Kang JU, Bergles DE. 2014. Norepinephrine controls astroglial responsiveness to local circuit activity. Neuron 82:1263–1270.

Petravicz J, Boyt KM, McCarthy KD. 2014. Astrocyte IP3R2-dependent Ca(2+) signaling is not a major modulator of neuronal pathways governing behavior. Front Behav Neurosci 8:384.

Petzold GC, Murthy VN. 2011. Role of astrocytes in neurovascular coupling. Neuron 71:782–797.

Piet R, Poulain DA, Oliet SH. 2002. Modulation of synaptic transmission by astrocytes in the rat supraoptic nucleus. J Physiol Paris 96:231–236.

Ramón y Cajal S. 1899. Textura del sistema nervioso del hombre y de los vertebrados. Madrid: Imprenta y libreria de Nicolas Moya.

Rose CR, Karus C. 2013. Two sides of the same coin: sodium homeostasis and signaling in astrocytes under physiological and pathophysiological conditions. Glia 61:1191–1205.

Schummers J, Yu H, Sur M. 2008. Tuned responses of astrocytes and their influence on hemodynamic signals in the visual cortex. Science 320:1638–1643.

Sherman SM, Guillery RW. 1998. On the actions that one nerve cell can have on another: distinguishing "drivers" from "modulators". Proc Natl Acad Sci U S A 95:7121–7126.

Shigetomi E, Jackson-Weaver O, Huckstepp RT, O'Dell TJ, Khakh BS. 2013. TRPA1 channels are regulators of astrocyte basal calcium levels and long-term potentiation via constitutive D-serine release. J Neurosci 33:10143–10153.

Sibille J, Pannasch U, Rouach N. 2014. Astroglial potassium clearance contributes to short-term plasticity of synaptically evoked currents at the tripartite synapse. J Physiol 592:87–102.

Sibille J, Dao Duc K, Holcman D, Rouach N. 2015. The neuroglial potassium cycle during neurotransmission: role of Kir4.1 channels. PLoS Comput Biol 11:e1004137.

Sirevaag AM, Greenough WT. 1991. Plasticity of GFAP-immunoreactive astrocyte size and number in visual cortex of rats reared in complex environments. Brain Res 540:273–278.

Sloan SA, Barres BA. 2014. Mechanisms of astrocyte development and their contributions to neurodevelopmental disorders. Curr Opin Neurobiol 27:75–81.

Srinivasan R, Huang BS, Venugopal S, Johnston AD, Chai H, Zeng H, Golshani P, Khakh BS. 2015. Ca(2+) signaling in astrocytes from Ip3r2(-/-) mice in brain slices and during startle responses in vivo. Nat Neurosci 18:708–717.

Stokum JA, Gerzanich V, Simard JM. 2016. Molecular pathophysiology of cerebral edema. J Cereb Blood Flow Metab 36:513–538.

Stork T, Sheehan A, Tasdemir-Yilmaz OE, Freeman MR. 2014. Neuron-glia interactions through the Heartless FGF receptor signaling pathway mediate morphogenesis of Drosophila astrocytes. Neuron 83:388–403.

Theodoric N, Bechberger JF, Naus CC, Sin WC. 2012. Role of gap junction protein connexin43 in astrogliosis induced by brain injury. PLoS One 7:e47311.

Theodosis DT, Trailin A, Poulain DA. 2006. Remodeling of astrocytes, a prerequisite for synapse turnover in the adult brain? Insights from the oxytocin system of the hypothalamus. Am J Physiol Regul Integr Comp Physiol 290:R1175–1182.

Thrane AS, Rangroo Thrane V, Zeppenfeld D, Lou N, Xu Q, Nagelhus EA, Nedergaard M. 2012. General anesthesia selectively disrupts astrocyte calcium signaling in the awake mouse cortex. Proc Natl Acad Sci U S A 109:18974–18979.

Tong X, Ao Y, Faas GC, Nwaobi SE, Xu J, Haustein MD, Anderson MA, Mody I, Olsen ML, Sofroniew MV, Khakh BS. 2014. Astrocyte Kir4.1 ion channel deficits contribute to neuronal dysfunction in Huntington's disease model mice. Nat Neurosci 17:694–703.

Tsai HH, Li H, Fuentealba LC, Molofsky AV, Taveira-Marques R, Zhuang H, Tenney A, Murnen AT, Fancy SP, Merkle F, Kessaris N, Alvarez-Buylla A, Richardson WD, Rowitch DH. 2012. Regional astrocyte allocation regulates CNS synaptogenesis and repair. Science 337:358–362.

Usrey WM, Sceniak MP, Chapman B. 2003. Receptive fields and response properties of neurons in layer 4 of ferret visual cortex. J Neurophysiol 89:1003–1015.

Van Hooser SD. 2007. Similarity and diversity in visual cortex: is there a unifying theory of cortical computation? Neuroscientist 13:639–656.

Wang X, Lou N, Xu Q, Tian GF, Peng WG, Han X, Kang J, Takano T, Nedergaard M. 2006. Astrocytic Ca2+ signaling evoked by sensory stimulation in vivo. Nat Neurosci 9:816–823.

Weber B, Keller AL, Reichold J, Logothetis NK. 2008. The microvascular system of the striate and extrastriate visual cortex of the macaque. Cereb Cortex 18:2318–2330.

Weliky M, Bosking WH, Fitzpatrick D. 1996. A systematic map of direction preference in primary visual cortex. Nature 379:725–728.

Wilhelmsson U, Bushong EA, Price DL, Smarr BL, Phung V, Terada M, Ellisman MH, Pekny M. 2006. Redefining the concept of reactive astrocytes as cells that remain within their unique domains upon reaction to injury. Proc Natl Acad Sci U S A 103:17513–17518.

Xu G, Wang W, Kimelberg HK, Zhou M. 2010. Electrical coupling of astrocytes in rat hippocampal slices under physiological and simulated ischemic conditions. Glia 58:481–493.

Xu G, Wang W, Zhou M. 2014. Spatial organization of NG2 glial cells and astrocytes in rat hippocampal CA1 region. Hippocampus 24:383–395.

Yasuda Y, Tateishi N, Shimoda T, Satoh S, Ogitani E, Fujita S. 2004. Relationship between S100beta and GFAP expression in astrocytes during infarction and glial scar formation after mild transient ischemia. Brain Res 1021:20–31.

Yu H, Farley BJ, Jin DZ, Sur M. 2005. The coordinated mapping of visual space and response features in visual cortex. Neuron 47:267–280.